Deconvolution of partially compensated solar images from additional wavefront sensing

NORIAKI MIURA,[1] AKIRA OH-ISHI,[1] SUSUMU KUWAMURA,[1] NAOSHI BABA,[2,3] SATORU UENO,[4] YOSHIKAZU NAKANANI,[4] AND KIYOSHI ICHIMOTO[4]

[1] *Department of Computer Sciences, Kitami Institute of Technology, 165 Koen-cho, Kitami, Hokkaido 090-8507, Japan*
[2] *Faculty of Engineering, Hokkaido University, Sapporo, Hokkaido 060-8628, Japan*
[3] *Muroran Institute of Technology, Muroran, Hokkaido 050-8585, Japan*
[4] *Hida Observatory, Graduate School of Science, Kyoto University, Kamitakara, Takayama, Gifu 506-1314, Japan*
**Corresponding author: miuranr@mail.kitami-it.ac.jp*

Received XX Month XXXX; revised XX Month, XXXX; accepted XX Month XXXX; posted XX Month XXXX (Doc. ID XXXXX); published XX Month XXXX

A technique of restoring solar images partially compensated with adaptive optics is developed. An additional wavefront sensor is installed in an adaptive optics system to acquire residual wavefront information simultaneously to a solar image. A point spread function is derived from the wavefront information and used to deconvolve the solar image. Successful image restorations are demonstrated when estimated point spread functions have relatively high Strehl ratios.

OCIS codes: *(100.1830)Deconvolution; (010.7350) Wave-front sensing; (100.3020) Image reconstruction-restoration; (010.1080) Active or Adaptive optics.*

http://dx.doi.org/10.1364/AO.99.099999

1. INTRODUCTION

Adaptive optics (AO) systems are being used for solar observation in various observatories [1-3]. We are also developing an AO system for the 60-cm domeless solar telescope at the Hida Observatory in Japan [4-6], which will be used for various purposes from near ultra violet to near infrared. It is, however, hard to attain full compensation especially in shorter wavelength because of severer influence of turbulence. To improve astronomical images degraded by turbulence, various image processing techniques are successfully used, such as the speckle masking method [7] and the phase diversity method [8]. However, since the speckle masking method requires hundred of images, heavy computational-cost and low temporal-resolution cannot be avoided. In the phase diversity method, a nonlinear optimization procedure is needed to derive a restored image from focused and defocused solar data.

Primot et al. [9] developed a technique of deconvolution from wavefront sensing (DFWS). In the technique, an image from a Shack-Hartmann (SH) wavefront sensor is also acquired simultaneously to a target image from a scientific camera. We hereafter refer the former to as an SH image, which contains the array of sub-images with local shifts. Deconvolution is statistically done in spatial frequency domain as $O=\langle IP\rangle/\langle|P|^2\rangle$, where O and I are spectra of an object and an observed image, respectively, P is an optical transfer function derived from the wavefront information, and <> denotes the ensemble average. Rimmele and Radick [10] applied the DFWS technique to solar images, and showed it to be useful to the restoration of solar images. They used a Wiener filter in the deconvolution procedure differently from the original DFWS technique. In the Wiener filter, signal-to-noise (SN) ratios of an observed image over the frequency domain are required, which are usually unknown. They used a priori knowledge on an object to estimate the SN ratios, and averaged 5-10 deconvolution results to improve the image quality.

We apply the DFWS technique to improving solar images partially corrected by AO [11]. We add another SH wavefront sensor into an AO system to obtain information on residual wavefront phases. The following points were considered in designing our method:

(a) Some solar structures drastically change in time. Therefore, time interval for data acquisition should be as short as possible, and restoration from a single-shot image must be ideal if possible. Therefore, we here aim at restoration from a single solar image. For our sake, we decided to adopt the Richardson-Lucy (RL) deconvolution method [12,13] because of the unnecessity of estimating unknown frequency-domain SN ratios used in the Wiener filter.

(b) In even solar observations, exposures longer than a few milliseconds are frequently used, because narrow-band filters like the Lyot filter give us significant information on solar structures

and behaviors. However, especially in poor seeing cases, we sometimes experience image variation faster than such times, and can no longer consider a point spread function (PSF) to be stable during exposure. Therefore, we design our system such that the additional wavefront sensor acquires a number of SH images during the exposure of a solar image. From the SH images, we derive a PSF over the exposure time, and deconvolve a solar image by it.

We describe the details of our experimental system and technique in section 2 and 3, and show restoration results of solar images observed at the Hida Observatory in Japan, in section 4.

2. OBSERVATIONAL SYSTEM

Figure 1 shows the layout of our experimental system [4,5]. The incident light to the system is relayed with sets of lens, and then is sequentially reflected with the tip-tilt mirror and the deformable mirror, which lie on conjugate planes of the entrance pupil. Parts of the light are split to be fed to the wavefront and tip-tilt sensing cameras. The deformable mirror used has 97 electromagnetic actuators and is featured with good linearity, no hysteresis and large stroke. The mirror is driven with modal-control operation. The AO system consists of two independent closed-loop units of correcting overall image shifts and wavefront errors, being individually operated by two standard personal computers.

In the wavefront sensor in the AO loop, referred to as WF-sensor 1, 56 subapertures on 10x10-microlens array were used to cover just a conjugate pupil image, which corresponded to the 6cm sampling over the telescope aperture. The WF-sensing camera 1 was a CMOS-type with image acquisition of 4000 fps (256x256). Each sub-image on a SH image had 25x25 pixels and the field of view (FOV) of 14.3x14.3". Wavefront phases were expanded with twenty Zernike polynomials.

We added another wavefront sensor, referred to as WF-sensor 2, for obtaining residual wavefront information. A merit of using an additional sensor is the possibility of raising the accuracy of measured wavefront phases more than that in AO loop, because we can use more subapertures, larger image sizes, and/or more number of polynomials without interfering AO behavior. In the WF-sensor 2, we used 116 subapertures on 14x14 microlens for wavefront measurement, while we set the image size to 256x256 the same as in WF sensor 1. The image acquisition with the size allowed us to observe the variation of PSFs with the highest speed. Although the number of pixels per a subaperture was fewer than that of WF-sensor 1, the use of more subapertures and orthogonal functions enabled the estimation of PSFs with better accuracy.

As orthogonal functions, we used 100 Karhunen-Loève (KL) ones. Although we followed the way in the reference papers [14, 15], we newly derived annular KL functions for the pupil of the domeless solar telescope by restricting the region of orthogonal integration. By virtue of using KL functions instead of Zernike polynomials, we could reduce fitting errors on the aperture edge when using a large number of orthogonal functions. Since the KL functions became available after the observation, we did not use them in the AO loop.

When acquiring data, we apply a trigger signal to both a science camera and the additional wavefront sensor to simultaneously capture an object and wavefront information. The camera in the WF-sensor 2 is same model as in the AO loop. The use of such a high-speed camera usually yields multiple SH images for the exposure of a single solar image.

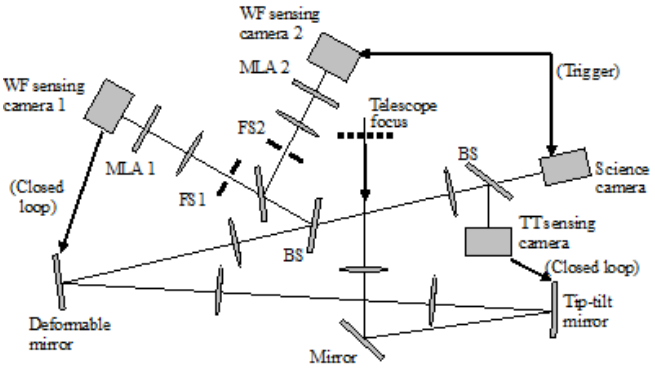

Figure 1. Optical layout of adaptive optics system including data acquisition system

3. IMAGE PROCESSING PROCEDURE

A solar image partially compensated through AO is modeled as

$$i(x,y) = o(x,y) * h(x,y)\,, \tag{1}$$

where $o(x,y)$ and $h(x,y)$ are an object and a PSF. The asterisk * denotes convolution. For the exposure of a solar image, M SH images are captured as samples of temporal wavefront variation. The m-th SH image is processed to obtain m-th wavefront phases

$$\phi_m(u,v) = \sum_{j=1}^{J} a_j K_j(u,v)\,, \tag{2}$$

similarly to in AO loop: shifts of a sensing target on each sub-image are detected with the cross-correlation procedure, and then the coefficients $\{a_j\}$ of the KL functions $K_j(u,v)$ are estimated from the measured shifts. The number of functions to be used for expansion, J, should be smaller than the number of subapertures.

Once wavefront phases are derived, an m-th instantaneous PSF $h_m(x,y)$ is calculated under the assumption of constant Fourier amplitude as

$$h_m(x,y) = \left| \boldsymbol{F}^{-1}\{\exp[i\phi_m(u,v)]\} \right|^2, \tag{3}$$

where $\boldsymbol{F}^{-1}\{\}$ denotes the inverse Fourier transform. A long-exposure PSF corresponding to an observed solar image is estimated as a simple shift-and-add of the instantaneous PSFs:

$$\tilde{h}(x,y) = \frac{1}{C} \sum_{m=1}^{M} h_m(x - x_m, y - y_m)\,, \tag{4}$$

where C is a normalizing factor for making the total intensity of $\tilde{h}(x,y)$ unity, and (x_m, y_m) is the m-th position of a target on the reference sub-image, which is measured with the correlation between the target on the first frame and that on the m-th frame. The exposure time of a SH image is so short that atmospheric turbulence is frozen. Therefore, the SH image can reflect instantaneous wavefront information well, and then $h_m(x,y)$ will be reliable. As a consequence, $\tilde{h}(x,y)$ can be a good estimate of $h(x,y)$.

When a PSF estimate is available, various popular deconvolution methods can be used for image restoration. In the

RL method adopted here, a (k+1)-th estimate of the object is given by

$$\tilde{o}^{(k+1)}(x,y)=\tilde{o}^{(k)}(x,y)\cdot\left[\frac{i(x,y)}{\tilde{o}^{(k)}(x,y)*\tilde{h}(x,y)}\otimes\tilde{h}(x,y)\right], \quad (5)$$

where $\otimes$ denotes correlation. As the initial estimate $\tilde{o}^{(0)}(x,y)$, we used a uniform-intensity image whose total intensity is same as that of $i(x,y)$. We monitor the behavior of the algorithm using an error metric:

$$E(k)=\sum_{(x,y)}\left[\frac{i(x,y)}{\tilde{o}^{(k)}(x,y)*\tilde{h}(x,y)}-1\right]^2. \quad (6)$$

The first term in the bracket is the ratio of the observed solar image to its estimate, which also appears in Eq. (5). If the estimated image converges to the observed one, then $E(k)\rightarrow 0$. In this case, the estimate $\tilde{o}^{(k)}$ no longer changed. Referring $E(k)$, we determine the iteration number to be terminated.

4. OBSERVATION AND RESULTS

Observations were conducted using the 60-cm domeless solar telescope of the Hida Observatory on 4 June, 2013. The science camera used was the Hamamatsu C4880-80 specified with 656x494 pixels, readout frequency of 28 Hz, and 12 bit dynamic range. The observational wavelength and bandwidth were 431 and 4 nm, respectively. The exposure time of solar images was 8.2 ms, while the frame rate of the wavefront sensor was 4000 Hz. Therefore, M=32 SH images were captured for the exposure of a solar image.

Figure 2 shows an example of AO correction: solar images observed (a) with and (b) without AO. The FOV is 44.1x35.2 arcsec. The AO system operated with the control frequency of 1100 Hz in this observation. The target for the wavefront sensing was the lower edge of the center sunspot. Structures become fine over the image in Fig. 2(a), but the effect of restoration is not so obvious on far regions from the target, especially on the lower right corner.

We segmented a sub-image with 448x448 pixels around the target from an observed image, and apodized edge regions of 32 pixels as converged to the mean value of them. We then put it on the center of a 512x512 image whose pixel values were initialized to the mean value. The resultant 512x512 image was used in the deconvolution process. Only the central 384x384 region of the restored image will be displayed in the following results.

Figure 3(a) is one of SH images observed with the additional wavefront sensor with 14x14 microlens. We set the target for wavefront sensing to the same one as in AO loop. From a SH image, we derived 100 KL-coefficients and then reconstructed wavefront phases. The wavefront phase map derived from Fig. 3(a) is shown in (b). The maximum (white) and minimum (black) were 3.16 and -3.84 rad, respectively, after the removal of piston and tilt components. An instantaneous PSF was derived from such a wavefront phase map.

The strip images in Fig. 4 show the time sequences of eight instantaneous PSFs with time interval of 1 ms. Reformation of the mirror surface was expected between a PSF and the next because the AO system operated with 1100 Hz. When the AO certainly worked well as in the cases of (a) and (b), the PSFs were almost unchanged for the exposure of 8.2 ms in spite of the reformation of the mirror surface. On the other hand, Fig. 4(c) demonstrates the temporal variations of instantaneous PSFs. We understand this case as a case in which AO did not work as expected because of severe seeing beyond the ability of AO. In Fig. 4(d), the shapes of instantaneous PSFs undesirably changes from a single peak to twin peaks.

The right images in Fig. 4 show long-exposure PSFs corresponding to their left strip images. We regard that the PSFs in (a) and (b) consist of a single core and a halo. This is like a typical PSF through an AO system. On the other hand, no core exists in Fig. 4(c) and the peak is elongated in Fig. 4(d). The Strehl ratios of the long-exposure PSFs were (a) 0.126, (b) 0.152, (c) 0.029, and (d) 0.115, respectively. We found that a Strehl ratio more than 0.12 is necessary for successful restoration in the present experimental situation.

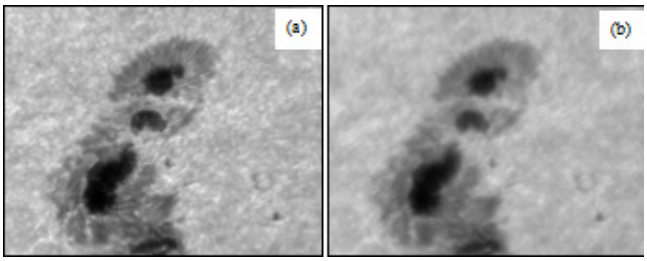

Figure 2. Solar images observed (a) with and (b) without AO.

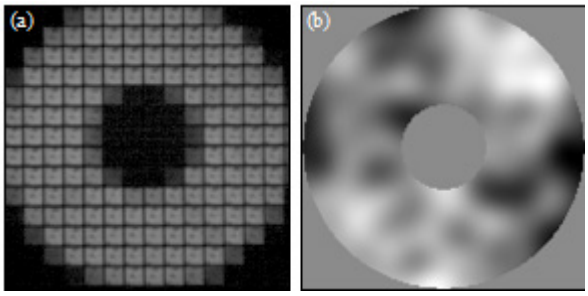

Figure 3. (a) An image acquired with an additional Shack-Hartmann sensor, and (b) the wavefront phase map derived from (a). White is the maximum and black is the minimum..

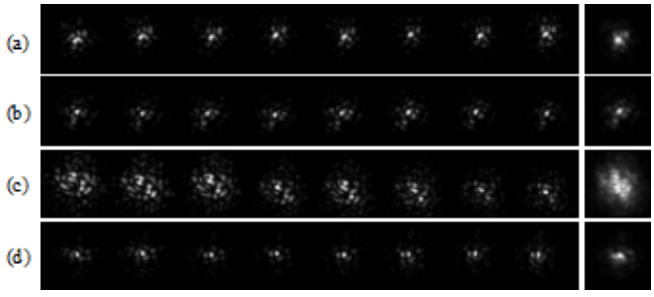

Figure 4. Time sequences of estimated instantaneous PSFs (left strip images) and long-exposure PSFs (right images) in cases of (a),(b) successful and (c),(d) failure image restorations. Refer Table 1 in detail.

Figure 5 plots the logarithm of $E(k)$ when deconvolving the solar image to be appeared in Fig. 6(a) by the long-exposure PSF in Fig. 4(a). The error metric greatly decreases within a few iterations and then gradually converges monotonically. The $\log(E(k))$ profiles were always similar in other experiments. By visually inspecting restored images, we regarded the convergence to be sufficient when $E(k)$ is less than 0.01. We thus decided to terminate the algorithm at 200 iterations.

We carried out image restoration of fourteen solar images as summarized in Table 1. Only two cases were successful, because the seeing conditions were not good on the observational day. Figure 6 shows the deconvolution results in (a), (b) successful cases and (c),(d) failure cases, where PSFs used in deconvolution are of Fig. 4(a)-(d), respectively. In (e) and (f), structures become finer and the image contrast becomes higher than (a) and (b). On the other hand, in failure case (g), image contrast is raised but fine structures are not restored. This is because high spatial frequency components in the observed image were lost due to sever image degradation. Although the image in the other case (h) shows fine structures, grain-like artifacts are notable. We think that high frequency components remained somewhat but were insufficient for successful image restoration.

To visualize the effect of image restoration, we calculated contrast of an image using a moving window with 50x50 pixels, where it is defined as the ratio of the deviation to the mean value inside the window. Figures 7(a) and (b) are the contrast maps of the images in Fig. 6(a) and (e). As can be seen, the contrast has large values around the sunspots, in particular on edges between umbra and penumbra and between penumbra and granules. After deconvolution, there are relatively-large contrast values on granule regions. The maximum values of the contrast were (a) 0.403 and (b) 0.480. Figure 7(c) shows the increment of (b) from (a). Restoration is notable near the target of wavefront sensing, while its effect is not so large on regions far from the target because of anisoplanatism.

Table 1. Summary of PSF estimation and image restoration

No.	Observation Time(JST)	Restored image quality	PSF Strehl ratio	Corresponding figures
1	08:04:12	Not fine	0.031	
2	08:05:54	Not fine	0.037	
3	08:06:36	Not fine	0.037	
4	08:08:05	Not fine	0.073	
5	08:08:48	Artifacts	0.115	4(d), 6(d)(h)
6	08:10:09	Not fine	0.039	
7	08:14:02	Artifacts	0.063	
8	08:14:49	Not fine	0.029	4(c), 6(c)(g)
9	08:15:27	Not fine	0.036	
10	08:16:13	OK	0.126	3, 4(a), 5, 6(a)(e),7
11	08:21:33	Not fine	0.043	
12	08:25:33	Artifacts	0.064	
13	08:35:47	Not fine	0.034	
14	08:48:18	OK	0.152	4(b), 6(b)(f)

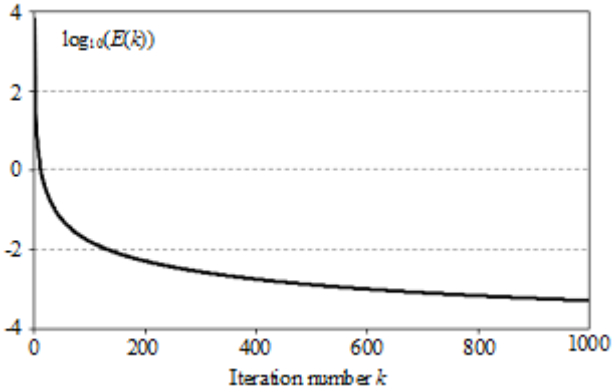

Figure 5. Error metric versus iteration number

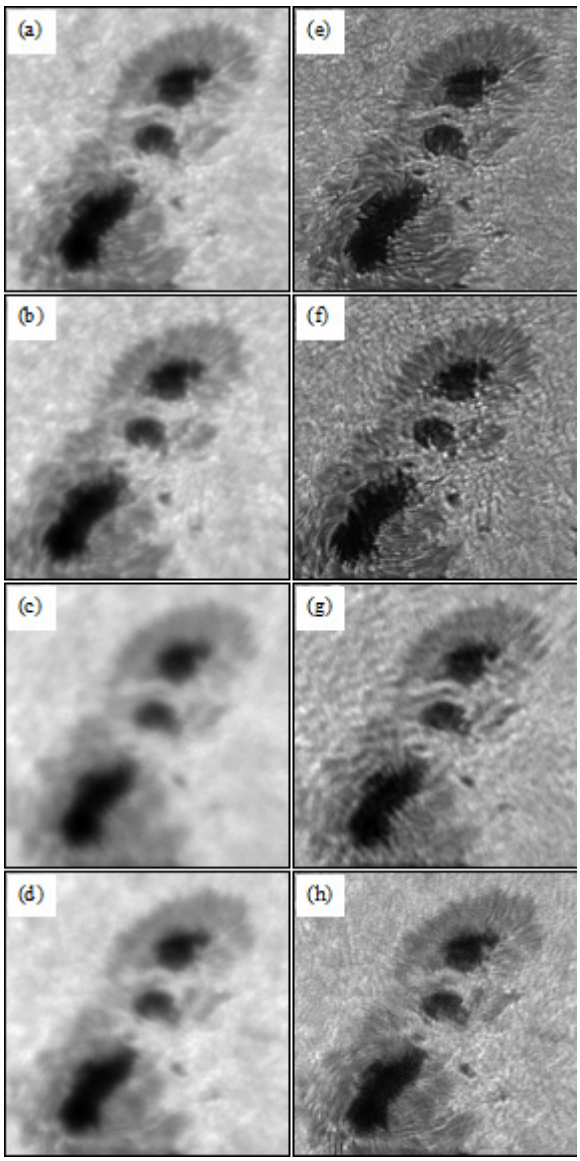

Figure 6. (a)-(d) Solar images observed through AO at different times (see Table 1), (e)-(h) deconvolution results of (a)-(d) using PSFs in Fig. 4(a)-(d), respectively.

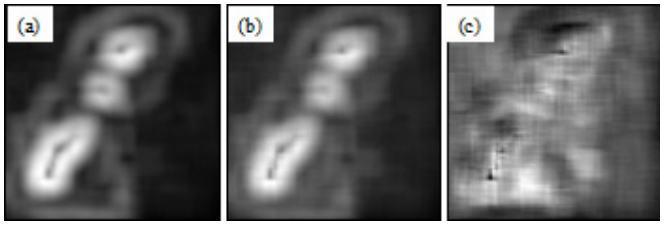

Figure 7. Contrast maps of images (a) before and (b) after deconvolution, which correspond to Fig. 6(a) and (e), respectively. (c) Increment of contrast from (a) to (b).

5. SUMMARY AND DISCUSSIONS

We developed a technique of improving solar images partially compensated by AO on the basis of the DFWS technique. We added another wavefront sensor into our AO system and implemented simultaneous acquisition of a solar image and wavefront information. Deriving a PSF from the wavefront information, we deconvolved the solar image by it. We applied our technique to solar data observed at the Hida Observatory, and confirmed the improvement of image contrast and resolution in restored solar images.

We noticed that PSFs estimated in successful cases had larger Strehl ratios than those in failure cases. In successful cases, the temporal variation of instantaneous PSFs was relatively stable during the exposure time and a long-exposure PSF derived from them consisted of a core and a halo. A solar image observed with such a PSF preserved high-spatial frequency components, and a restored image as a result demonstrated fine structures. In our experimental system, Strehl ratios of more than 0.12 should be attained by AO for successful image restoration.

To obtain PSFs with higher Strehl ratios, we must raise the performance of the AO system. We theoretically estimated that the major source of residual wavefront errors was time delay in our experimental AO system. The limited numbers of subapertures and actuators had almost same contributions to the wavefront errors. We are developing a new full-scaled AO system with higher performances [6]. Using the new AO system, we will make further experiments to state our solar DWFS technique more specifically, not only for the Strehl ratio but also for other factors, such as the SN ratio and dynamic range of the science camera.

When estimating instantaneous PSFs using Eq. (4), we assumed the constant wavefront amplitude. Of course, this is strictly not true, especially under bad seeing conditions. If we can use the amplitude information in our technique, estimated PSFs will become more precise. We plan to upgrade our system so as to measure the intensity variation on the pupil plane simultaneously to capturing a SH image.

A limited field of correction due to the anisoplanatism, as shown at the end of section 4, is a significant problem for the study of large-scaled dynamic phenomena on the solar surface. Our solar DFWS technique is extensible to wide-field restoration because the RL technique is easily modified to the form of using shift-variant PSFs. In such shift-variant restoration, the key point is how to gather PSFs on various positions over a FOV. We consider that the same wavefront sensor as used in solar multi-conjugate AO systems [3,16] will be useful.

Funding Information. This work was partly supported by Grant-in-Aid for Challenging Exploratory Research from the Japan Society for the Promotion of Science (No. 24654045).

References

1. T. R. Rimmele, "Recent advances in solar adaptive optics," Proc. SPIE, **5490**, 34-46 (2004).
2. S. Shunko, N. Gorceix, S. Choi, A. Kellerer, W. Cao, P. R. Goode, V. Abramenko, K. Richards, T. R. Rimmele, and J. Marino, "AO-308: the high-order adaptive optics system at Big Bear Solar Observatory," Proc. SPIE, **9148**, 9148-35 (2014)
3. D. Schmit, T. Berkefeld, F. Heidecke, A. Fischer, O. von der Lühe, and D. Soltau, "GREGOR MCAO looking at the sun," Proc. SPIE, **9148**, 9148-1T (2014).
4. N. Miura, Y. Noto, S. Kato, F. Yokoyama, S. Kuwamura, N. Baba, Y. Hanaoka, S. Nagata, S. Ueno, R. Kitai, K. Ichimoto, and H. Takami, "Solar Adaptive Optics System Using an Electromagnetic Deformable Mirror," Opt. Rev., **16**, 558-561 (2009).
5. N. Miura, J. Miyazaki, S. Kuwamura, N. Baba, Y. Hanaoka, M. Yamaguchi, S. Ueno, Y. Nakatani, S. Nagata, R. Kitai, K. Ichimoto, and H. Takami, "Solar adaptive optics at the Hida Observatory: latest achievements of current system and design on new system," Proc. SPIE, **8447**, 8447-162 (2012).
6. N. Miura, A. Oh-ishi, S. Aoki, H. Mogaki, S. Kuwamura, N. Baba, Y. Hanaoka, M. Yamaguchi, S. Ueno, Y. Nakatani, S. Nagata, R. Kitai, and K. Ichimoto, "Development of a new solar adaptive optics system at the Hida Observatory," Proc. SPIE, **9148**, 9148-31 (2014).
7. A. F. Lohmann, G. Weigelt, and B. Wirnitzer, "Speckle Masking in Astronomy: triple correlation theory and applications," Appl. Opt., **22**, 4028-4037 (1983).
8. M. G. Löfdahl and G. B. Scharmer, "Wavefront sensing and image restoration from focused and defocused solar images," A&A Suppl., **107**, 243-264 (1994).
9. J. Primot, G. Rousset, and J. C. Fontanella, "Deconvolution from wave-front sensing: a new technique for compensating turbulence-degraded images," JOSAA, **7**, 1598-1608 (1990).
10. T. R. Rimmele and R. R. Radick, "Deconvolving solar images using a Shack-Hartmann wavefont sensor," Proc. SPIE, **3353**, 1014-1021 (1998).
11. N. Miura, A. Oh-ishi, S. Kuwamura, N. Baba, S. Ueno, Y. Nakatani, and K. Ichimoto, "Solar image improvement based on deconvolution using additional wavefront sensor," Imaging and Applied Optics Technical Digest, JT5A.29 (2015, OSA, Arlington, USA).
12. W. H. Richardson, "Bayesian-based iterative method of image restoration," JOSA, **62**, 55-59 (1972).
13. L. B. Lucy, "An iterative technique for the rectification of observed distributions," AJ, **79**, 745-754 (1974).
14. G.-m. Dai, "Wavefront simulation for atmospheric turbulence," Proc. SPIE, **2302**, 62-72 (1994).
15. G.-m. Dai, "Modal compensation of atmospheric turbulence with the use of Zernike polynomials and Karhunen-Loeve functions," JOSAA, **10**, 2182-2193 (1995).
16. T. R. Rimmele, F. Woeger, J. Marino, K. Richards, S. Hegwer, T. Berkefeld, D. Soltau, D. Schmidt, T. Waldmann, "Solar multiconjugate adaptive optics at the Dunn Solar Telescope," Proc. SPIE, **7736**, 773631 (2010).